Oxygen vacancy induced electronic structure modification of KTaO₃

Shashank Kumar Ojha [ORCID],[1,*] Sanat Kumar Gogoi [ORCID],[1,*] Prithwijit Mandal [ORCID],[1] S. D. Kaushik,[2] J. W. Freeland [ORCID],[3]
M. Jain [ORCID],[1,†] and S. Middey [ORCID][1,‡]

[1]*Department of Physics, Indian Institute of Science, Bengaluru 560012, India*
[2]*UGC-DAE Consortium for Scientific Research Mumbai Centre, R5 Shed, Bhabha Atomic Research Centre, Mumbai 400085, India*
[3]*Advanced Photon Source, Argonne National Laboratory, Argonne, Illinois 60439, USA*

The observation of a metallic interface between band insulators LaAlO₃ and SrTiO₃ has led to massive efforts to understand the origin of the phenomenon as well as to search for other systems hosting such two-dimensional electron gases (2-DEGs). However, the understanding of the origin of the 2-DEG is very often hindered as several possible mechanisms such as polar catastrophe, cationic intermixing, and oxygen vacancy (OV) can be operative simultaneously. The presence of a heavy element makes the KTaO₃ (KTO) based 2-DEG a potential platform to investigate spin-orbit coupling driven novel electronic and magnetic phenomena. In this work, we investigate the sole effect of OV in KTO, which makes KTO metallic. O K-edge x-ray absorption spectroscopy measurements find that OV dopes electrons in Ta t_{2g}^* antibonding states. Photoluminescence measurements reveal the existence of a highly localized deep midgap state in oxygen-deficient KTO. Our detailed *ab initio* calculations demonstrate that such deep midgap state arises due to the linear clustering of OVs around Ta. Our present work emphasizes that we must pay attention to the possible presence of OVs in interpreting emergent behavior of KTO-based heterostructures.

I. INTRODUCTION

SrTiO₃-based oxide heterostructures are hosts of several emergent phenomena such as two-dimensional electron gas (2-DEG), ferromagnetism, and superconductivity [1–9]. The larger carrier density ($\geqslant 10^{13}$–10^{14} cm^{-2} vs. 10^{10}–10^{12} cm^{-2}) and shorter confinement length (1–2 nm vs. 10 nm) of the carriers at the interface of these SrTiO₃ (STO) based 2-DEGs, compared to traditional semiconductor 2-DEGs, makes these systems attractive for device applications [3,10]. However, mobility of these STO-based heterostructures is significantly low compared to semiconductor 2-DEGs, prompting the search for non-STO-based 2-DEG systems [11]. Bulk KTaO₃ (KTO) is a wide-band-gap insulator ($E_g \sim 3.5$ eV) and has a lot of similarities with STO such as cubic structure and quantum paraelectricity [12]. Similarly to STO, electron doping makes KTO metallic and even superconducting at very low temperature [13–15]. The presence of heavy element Ta further offers the possibility of achieving new emergent phases due to strong spin-orbit coupling (SOC), leading to many experimental works on KTO-based heterostructures [16–25]. Comparable values of SOC strength with other energy scales in KTO leads to significant reconstruction of orbital symmetries at the surface [26], which can further result in nontrivial spin-orbital texturing of conduction electrons [27]. The presence of such unconventional spin texturing of conduction

electrons can be further utilized for engineering novel topological phenomena such as the topological Hall effect [28], making the KTO-based 2DEG a unique platform for topological spintronics applications [29].

Similarly to the controversial origin of the metallic behavior in the LaAlO₃/SrTiO₃ interface [30–37], the origin of the 2-DEG in KTO-based heterostructures has been linked to electronic reconstruction due to polar catastrophe [19,24], as well as oxygen vacancy (OV) formation [21]. While a higher carrier density has been achieved in the LaTiO₃/KTO interface as predicted by the polar catastrophe model [19], the presence of OVs within the KTO substrate is also highly probable due to the use of high-vacuum atmosphere during the growth.

In order to understand the sole effect of the OV without any involvement of polar catastrophe and cationic intermixing issues [20], we have deliberately introduced the OV in the KTO single crystal through thermal annealing in a reduced atmosphere. In contrast to the method of electron doping by Ar$^+$ bombardment, the present method does not damage the crystallinity of the sample [28] and results in metallic KTO. O K-edge x-ray absorption spectroscopy (XAS) measurements reveal electron doping in Ta t_{2g}^* bands. Interestingly, we detect the presence of a deep midgap state through photoluminescence (PL) measurements. Our deatiled *ab initio* calculations with isolated OVs find that each isolated OV donates 2 electrons which are doped into the conduction band, derived from Ta t_{2g}^* antibonding states, resulting in metallic behavior. We further find that linear clustering of OVs is more favorable than the formation of isolated OVs. Most importantly, our calculations predict that such clustering would lead to the

*These authors contributed equally.
†mjain@iisc.ac.in
‡smiddey@iisc.ac.in

formation of a deep, narrow midgap state between the fully filled valence band and partially occupied conduction band and explains the experimentally observed deep midgap state in oxygen-deficient KTO.

II. METHODOLOGY

The commercially available (Princeton Scientific Corporation) KTO (0 0 1) single crystal (5 mm × 5 mm × 0.5 mm) was sealed with Ti metal wire in a quartz tube under a vacuum of 10^{-4} bars [38]. This sealed tube was heated at 900 °C for 24 hr. Temperature-dependent dielectric measurement was carried out using an impedance analyzer from Keysight Technology Instruments (model No. E49908). Resistance was measured with wire-bonded Al contact in a van der Pauw geometry using a Helium Re-liquefier based 9 T physical property measurement system (Quantum Design). XAS measurement on the O K-edge at 300 K was carried out at the 4-ID-C beamline of the Advanced Photon Source, Argonne National Laboratory. PL spectra were collected with the Horiba LabRAM HR instrument under excitation with a 266 nm ultraviolet laser at room temperature.

The *ab initio* calculations were carried out using the QUANTUM ESPRESSO package [39]. The Perdew, Burke, and Ernzerhof generalized gradient approximation (PBE-GGA) was used for the exchange correlation functional [40]. We have also performed calculations using the hybrid functional of Heyd, Scuseria, and Ernzerhof (HSE) [41]. Optimized norm-conserving pseudopotentials [42–44] were used in all the calculations. The Brillouin zone was sampled with $8 \times 8 \times 8$ k points for the unit cell and the wave functions were expanded in plane waves with an energy up to 90 Ry. We have performed noncollinear density functional theory (DFT) calculations with fully relativistic pseudopotentials for the Ta atom to capture the effect of the strong SOC. Upon including an additional on-site Coulomb potential of 1.35 eV [45] on the Ta d orbitals, the qualitative conclusions remain unchanged. The structural relaxations were performed until the force on each atom was reduced to 0.07 eV/Å.

III. RESULTS AND DISCUSSION

Stoichiometric KTO with Ta^{+5} ions in the d^0 configuration is a band insulator. Owing to its incipient ferroelectric nature, it is characterized by a large dielectric constant at low temperature. This is evident from Fig. 1(a), where we plot the temperature-dependent dielectric constant (ϵ) and dielectric loss (tan δ) of the as-received pristine KTO single crystal. The values of ϵ and tan δ and their temperature dependencies are very similar to earlier works [46,47]. KTO, annealed in the presence of Ti wire, becomes metal as evident from the temperature-dependent sheet resistance (R_S) from 2 K to 300 K [Fig. 1(b)]. Upon reheating this sample in oxygen atmosphere, we found that it becomes insulating, establishing that the origin of the metallic behavior is related to the presence of OVs. The R_S of oxygen-deficient KTO at 300 K is about 2 orders of magnitude smaller compared to that of the 2-DEG behavior of LaTiO₃/KTaO₃ [19], EuO/KTaO₃ [21], and LaVO₃/KTaO₃ [24] heterostructures. Similarly, to the cases of thin films grown on KTO sub-
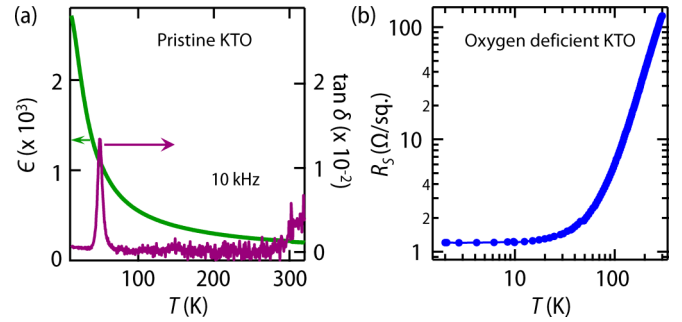

FIG. 1. (a) Temperature dependence of dielectric constant (ϵ) and dielectric loss (tan δ) of pristine KTO. (b) Temperature dependence of sheet resistance for oxygen-deficient KTO.

strates [19,21,24], R_S becomes temperature independent at low temperature due to the dominant contribution of electron scattering from defects [11,48]. Assuming single-band transport, we found carrier density $n_S \sim 2 \times 10^{15}$ cm^{-2} and electron mobility $\mu_e \sim 20$ cm^2/V s at room temperature from Hall effect measurement (not shown).

We have investigated the effect of OV on the electronic structure of KTO by O K-edge XAS, where one core electron from the O $1s$ state is excited to O $2p$ states [49]. In an ionic picture, such O $1s \rightarrow$ O $2p$ transition is not allowed as $2p$ orbitals are completely occupied for the O^{2-} ion. However, the strong hybridization between oxygen and other elements in a real material gives rise to a finite spectral weight of oxygen $2p$ character in the unoccupied density of states, which can be approximately described by O K-edge XAS [50]. Normalized XAS spectra, recorded in bulk sensitive total fluorescence yield (TFY) mode, have been compared in Fig. 2. To understand the origin of various features of these XAS spectra, the convoluted projected density of states (PDOS) of the O $2p$ states, obtained from density functional theory (discussed later in the paper), has been also plotted (for details see Sec. A of the Supplemental Material (SM) [51]). The first peak around 531.3 eV is due to transition to the states just above the Fermi level and primarily consists of the Ta $5d$ t_{2g} orbital, hybridized with O $2p$ orbitals [52]. The lower intensity of this peak in the oxygen-deficient sample, compared to the
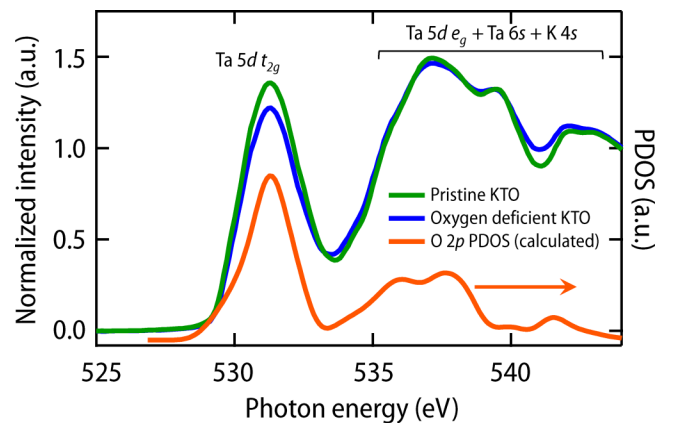

FIG. 2. O K-edge XAS spectra for pristine and oxygen-deficient KTO along with calculated O $2p$ PDOS for pristine KTO.
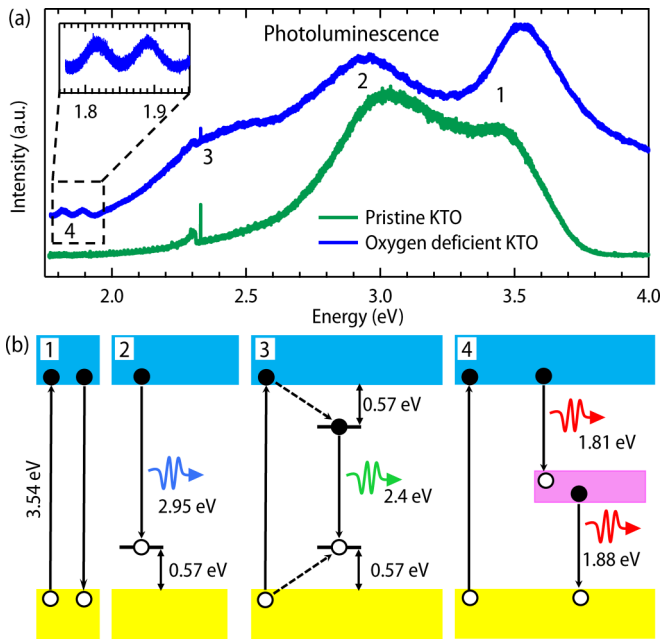
FIG. 3. (a) PL spectra of pristine and oxygen-deficient KTO. The inset shows the magnified view of midgap states around 1.8 eV. (b) The first panel corresponds to the near-band-edge emission. The second panel shows the recombination process between the excited electrons and the self-trapped excited holes. The third panel demonstrates the recombination process of excited holes and electrons in a self-trapped excited state. The fourth panel highlights the recombination process via defect band resulting in the peak around 1.8 eV in PL. Filled circle denotes electrons and open circle denotes holes.

FIG. 4. (a) Band structure of pristine KTO for a $2 \times 2 \times 2$ supercell. (b) Band structure of oxygen-deficient KTO ($KTaO_{2.875}$) for a $2 \times 2 \times 2$ supercell with single isolated oxygen vacancy. The Fermi level is marked with a solid orange line in both the panels.

pristine KTO, implies that some of the doped electrons have occupied Ta t_{2g}^* antibonding states, which is also concluded by our calculations shown later. The features from 534 eV to 544 eV are related to the transitions to the Ta $5d\ e_g$, Ta $6s$, and K $4s$ states hybridized with O $2p$.

In contrast to the carrier doping by elemental substitution at the A or B site in ABO_3 perovskites, OV creation not only dopes electrons to the system but can also lead to the formation of nondispersive midgap states [53]. As a result, some of the electrons are trapped in such midgap states and are localized around the vacancy in real space. In order to check the presence of such midgap state, we did PL measurement as this technique has been found to be very successful in locating the exact position of such defect states in oxygen-deficient STO [53–57]. Figure 3(a) shows the room-temperature PL spectra for the pristine and oxygen-deficient KTO. The corresponding mechanism for the peaks marked by 1, 2, 3, and 4 are shown in Fig. 3(b). The peak at 3.5 eV for the pristine sample corresponds to the near-band-edge emission. The position of this peak directly corresponds to the band gap of KTO and matches very well with the reported band gap from UV-visible spectroscopy [58]. Since this transition occurs from the bottom of the conduction band to the top of the valence band, this peak is also observed for oxygen-deficient KTO. KTO is an incipient ferroelectric [12] and has strong electron-phonon coupling [59]. In the presence of electron-phonon coupling, photogenerated electron and hole pairs are
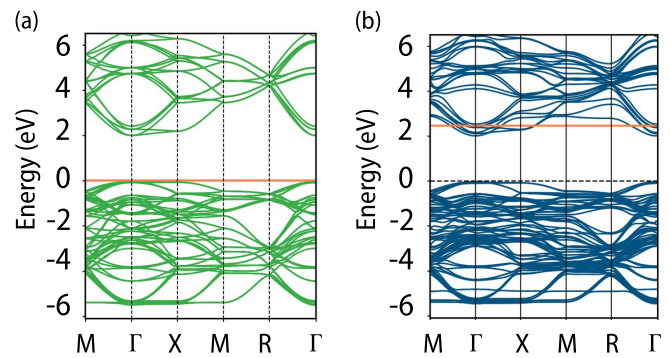
quickly trapped by phonons to form more stable self-trapped electron/hole states [60–62]. Recombination between these self-trapped electron and hole centers [third panel of Fig. 3(b)] leads to the "green" luminescence around 2.4 eV, which has been reported extensively in various perovskite oxides [63], including KTO [59]. This feature is strongly enhanced in the present case upon introduction of OV, as reported earlier for STO [64]. The peak at 2.95 eV can be attributed to the recombination of both excited and conduction electrons with the self-trapped holes [second panel of Fig. 3(b)].

Apart from these broad features, two new peaks have been observed at 1.81 eV and 1.88 eV [also see inset of Fig. 3(a)] in oxygen-deficient KTO. The origin of these peaks can be understood by considering a defect band, which would be at 1.8 eV below the minima of the conduction band [fourth panel of Fig. 3(b)]. This midgap state is separated equally from the valence and conduction band. The microscopic origin behind the existence of such midgap state in our samples will be discussed later in the paper.

To understand OVs' role in transforming the electronic properties of KTO, we have performed first-principles electronic structure calculations. The optimized lattice parameter of pristine cubic KTO was found to be 4.02 Å from PBE-GGA-approximated DFT calculations. This is very close to the experimentally reported value (3.989 Å [58]). The band structure of pristine KTO (for a $2 \times 2 \times 2$ supercell) is shown in Fig. 4(a). In this calculation, we computed the band gap to be 2.05 eV, which is also in good agreement with previous PBE-GGA-approximated DFT results [65–68]. Upon inclusion of an on-site Coulomb potential $U_{eff} = 1.35$ eV [45], the band gap increases to 2.1 eV (see Sec. C of the SM [51]). We have also found a split of the conduction bands at the $\Gamma(0, 0, 0)$ point by 400 meV, as reported before [16,17]. As a remedy to the underestimated band gap, we have further performed hybrid functional calculations using HSE, which yields a band gap of 3.6 eV (for details see Sec. E of the SM [51]), agreeing well with the experimentally reported band gap.

To examine OV's effect, we first considered isolated OV, as found by a scanning probe microscopy study on vacuum-annealed KTO [69]. For the calculations with an isolated
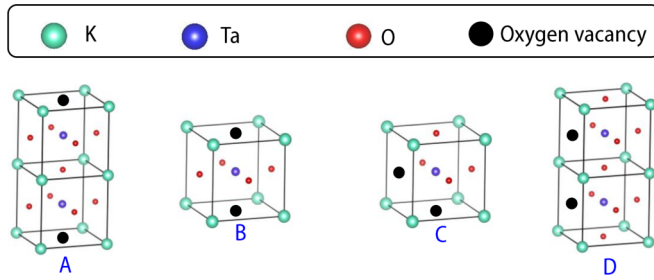
FIG. 5. Various relative configurations for oxygen divacancy in KTO, considered in our calculations.

OV within PBE-GGA, we considered a $2 \times 2 \times 2$ super-cell of KTO where one oxygen atom has been removed ($K_8Ta_8O_{24} \rightarrow K_8Ta_8O_{23}$). This corresponds to an OV concentration of 4.2%. As evident from the band structure plot shown in Fig. 4(b), the Fermi level is shifted to the conduction band, describing the experimentally observed metallic phase of oxygen-deficient KTO (density of states have been shown in Sec. B of the SM [51]). Our calculations find that one isolated OV donates two electrons to the conduction band. Among the 24 t_{2g} bands (3 t_{2g} bands for each Ta) in the conduction band manifold, six bands are partially filled by the 2 electrons. No localized defect state is found in the gap. This conclusion remains unaffected upon increasing the supercell size to $3 \times 3 \times 3$ (see Sec. D of the SM [51]).

Apart from the existence of isolated OV, perovskite compounds like STO also show a strong tendency for OV clustering [70–73]. To examine such clustering, we have considered a $2 \times 2 \times 4$ supercell containing two OVs with 4 different arrangements of OV (see Fig. 5 for the relative position of two OVs). To check the stability of such defect configurations, we have calculated the oxygen defect formation energy $E_f[mO_v]$, defined as [74]

$$E_f[mO_v] = E_{tot}[mO_v] + \frac{1}{2}m\mu_{O_2} - E_{tot}[0O_v]$$
$$+ q\left(E_{vbm}^{pristine} + \epsilon_F\right), \quad (1)$$

where $E_{tot}[mO_v]$ is the total energy of the system with m number of OV, $E_{tot}[0O_v]$ is the total energy of the pristine cell, μ_{O_2} is the chemical potential of the oxygen molecule, $E_{vbm}^{pristine}$ is the valance band maximum (VBM) for the pristine cell, ϵ_F is the Fermi energy, and q is the charge of the system. Formation energies for isolated OV as well as oxygen divacancy in different configurations in the neutral state ($q = 0$) are listed in Table I. The oxygen defect formation energies are in the same range that have been reported for other perovskite oxides [75,76] (also see Sec. F of the SM [51]). Moreover, we found that the linear oxygen divacancy around a Ta atom (configuration B) has the lowest formation energy, which suggests that the formation of a linear oxygen divacancy has a higher probability than two isolated vacancies.

Owing to the fact that the divacancies have lower formation energy compared to two isolated OVs, we also calculated the interaction energy E_{int} between the vacancies, which is defined as [71]

$$E_{int} = E_{tot}[2O_v] + E_{tot}[0O_v] - 2E_{tot}[1O_v]. \quad (2)$$

TABLE I. Table of formation energy per OV ($E_f[mO_v]/m$) and interaction energy (E_{int}) for different oxygen divacancy configurations (neutral) in KTO calculated using supercell $2 \times 2 \times 4$ and $4 \times 4 \times 4$ within PBE-GGA.

Configuration	$E_f[mO_v]/m$ (eV)		E_{int} (eV)	
	$2 \times 2 \times 4$	$4 \times 4 \times 4$	$2 \times 2 \times 4$	$4 \times 4 \times 4$
A	6.64	6.81	0.91	1.06
B	5.95	6.08	−0.49	−0.39
C	6.41	6.38	0.44	0.21
D	6.69	6.51	0.99	0.46
Single OV	6.84			

The negative (positive) sign of E_{int} specifies whether the interaction is attractive (repulsive). The interaction energies for different divacancy configurations are listed in Table I. As can be seen, configuration B, also known as an apical divacancy (OV-Ta-OV), has the most attractive interaction, implying that it is the most favorable among all divacancy configurations. Our calculations demonstrate that the linear vacancy clustering is favorable around Ta. It should be noted that even though configurations B and D have the same separation between the two vacancies, the E_{int} is very different. This implies that the location of the vacancies is also important and not just the relative distances.

The left panel of Fig. 6(a) shows the band structure plot of configuration B and PDOS right next to it with the same energy scale used in the band structure plot. Interestingly, apart from the partially occupied conduction bands, we find a highly localized defect band (marked in red), which is almost equidistant from the conduction and valence band edges. This explains the experimentally observed midgap state (which is almost equally separated from band edges) through PL measurement. Our conclusions remain unaffected upon inclusion of the on-site Coulomb potential (see Sec. C of the SM [51]).

The PDOS plot shows that the Ta $5d$ states mainly contribute to the defect band. The isosurface plot of the squared wave function of the defect band [Fig. 6(c)] is localized around the Ta atom in between the two OVs. Such electron localization around the vacancy site would lead to reduction of free carrier density. The $d_{3z^2-r^2}$ symmetry of this occupied defect band is related to the fact that the particular Ta atom with oxygen divacancy has a square planar environment locally, and the $d_{3z^2-r^2}$ is the lowest orbital for square planar crystal field [77]. A highly localized defect band has also been obtained in the band structure calculation for the configurations A and C (shown in Sec. G of the SM [51]).

We have also performed the calculations for a bigger supercell of size $4 \times 4 \times 4$ for all the divacancy configurations A, B, C, and D. As evident from Table I, the formation energies do not change much upon increasing the supercell size. The formation energy for configuration B again turns out to be the lowest among all the configurations, similarly to the case of the $2 \times 2 \times 4$ supercell. Further, the position of the defect state for the most stable divacancy configuration B remains unaffected upon increasing the supercell size to $4 \times 4 \times 4$ (see Sec. D of the SM [51]).
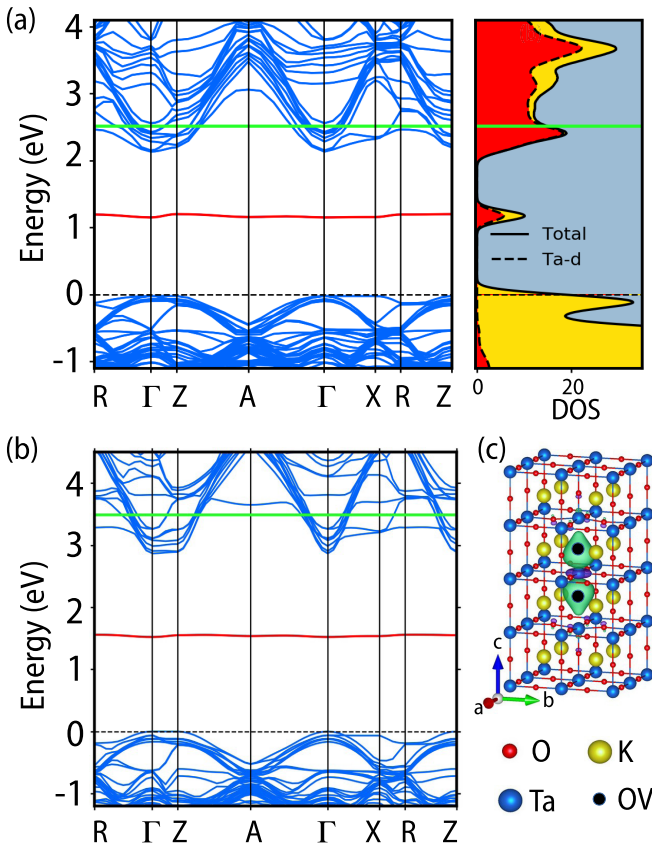
FIG. 6. (a) The PBE-GGA band structure of apical divacancy (configuration B) for a $2 \times 2 \times 4$ supercell is shown in the left panel. The defect band is marked with the color red. The right panel shows the projected density of states (PDOS) for Ta $5d$ orbitals in red and the total density of states in yellow. The Fermi level is shown in green. (b) The band structure calculated using HSE for a $2 \times 2 \times 4$ supercell with apical divacancy (configuration B). The defect band (≈ 1.5 eV from VBM) is shown in red and the Fermi level is marked by green. (c) The isosurface of the squared wave function for the defect band shown by green bubble for the configuration B (PBE-GGA calculation).

We have also monitored the position of defect state using the HSE functional for the divacancy configuration B. We found the midgap to be localized around 1.5 eV from VBM, shown in Fig. 6(b), close to the results we observed in PL measurement.

Till now we have investigated the formation energies for a neutral system with isolated OV and divacancies with different defect configurations. Since formation energy (E_f) is dependent on the charge state (q) of the system and position of the Fermi level (ϵ_F) [Eq. (1)], we have also computed $E_f[mO_v]$ per vacancy as a function of Fermi level position in different charge states (q) for the most favorable divacancy configuration B.

It is well known that [78–84] calculations of the charged defect system using periodic supercells can introduce some unphysical contributions into the defect formation energy calculations. From the calculations of the neutral divacancy system, one can see that 2 electrons are localized in the defect band discussed above, while 2 other electrons are in
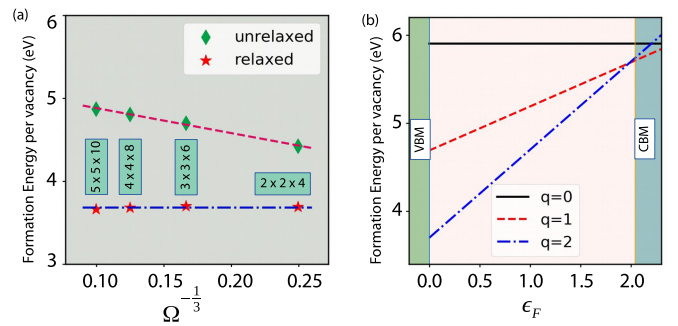

FIG. 7. (a) Formation energy per vacancy of an apical divacancy system as a function of system size (Ω) in the charge state $q = +2$. The considered supercell sizes are $5 \times 5 \times 10$, $4 \times 4 \times 8$, $3 \times 3 \times 6$, and $2 \times 2 \times 4$. (b) Formation energy diagram for different charge states of an apical divacancy in a $2 \times 2 \times 4$ supercell.

the conduction band manifold (see Fig. 6). Considering apical oxygen divacancy with +1 (+2) charge state in KTO, we remove 1 electron (2 electrons) from the conduction band manifold, which is smeared inside the whole cell. Thus, even though we are performing charged defect calculations, owing to the background charge compensation in periodic supercell calculations, we expect our calculated formation energies to behave close to the neutral system and to have a small electrostatic correction. To check the validity of the same, we have calculated the formation energies as a function of system size for the supercell of sizes $2 \times 2 \times 4$, $3 \times 3 \times 6$, $4 \times 4 \times 8$, and $5 \times 5 \times 10$ for the most stable divacancy configuration B (within PBE-GGA) shown in Fig. 7(a). The unrelaxed data have been fitted with a straight line, which goes as $\frac{1}{L}$ (where L is the measure of system length). However, once we allow the system to relax after creating the vacancies, the computed formation energies are invariant over system size variation, denoted by the red stars in Fig. 7(a). Moreover, the large dielectric constant of KTO is also responsible for the fact that the charged oxygen defects are screened form each other, which allow us to use comparatively small supercells in our calculations. Thus, we conclude that the $2 \times 2 \times 4$ supercell is sufficient to calculate the formation energies in this system. It shows that the correction needed in our formation energy calculations is negligible. The +1 charge state is metallic, and there is only one electron in the conduction band manifold. However, the +2 charge state is insulating in nature (see Secs. H and I of the SM [51]).

Figure 7(b) shows the different charge states for the apical divacancy case calculated using a $2 \times 2 \times 4$ supercell. We have found that the +2 charge state is more stable than the neutral one when the Fermi level resides inside the gap. We have also noticed a charge transition level at ≈ 1.9 eV (from the top of the valance band) from +2 to +1 charge state. In the experimental observations, we have found the system to be metallic. The *ab initio* calculations affirm that the Fermi level lies inside the conduction band. Thus, we expect the metallic states (+1 or neutral) to be more favorable. For the isolated oxygen vacancies also, it is found that the neutral state is more favorable [85]. Thus we conclude that despite various types of possible oxygen vacancies, the metallic system is more stable.

IV. CONCLUSION

To conclude, we have successfully demonstrated the sole effect of oxygen vacancy on the electronic structure of KTO. Pristine insulating KTO undergoes an insulator to metal transition (IMT) upon oxygen vacancy creation. DFT calculations show that IMT can be explained by just considering isolated oxygen vacancies. Further, our DFT calculations combined with photoluminescence measurements reveal that linear clustering of oxygen vacancies around the Ta atom leads to the formation of a very localized state within the band gap, which can result in fascinating magnetotransport phenomena in KTO [86].

[1] A. Ohtomo and H. Hwang, Nature (London) **427**, 423 (2004).

[2] N. Reyren, S. Thiel, A. Caviglia, L. F. Kourkoutis, G. Hammerl, C. Richter, C. Schneider, T. Kopp, A.-S. Rüetschi, D. Jaccard *et al.*, Science **317**, 1196 (2007).

[3] J. Mannhart, D. H. Blank, H. Hwang, A. Millis, and J.-M. Triscone, MRS Bull. **33**, 1027 (2008).

[4] J.-S. Lee, Y. Xie, H. Sato, C. Bell, Y. Hikita, H. Hwang, and C.-C. Kao, Nat. Mater. **12**, 703 (2013).

[5] A. Brinkman, M. Huijben, M. Van Zalk, J. Huijben, U. Zeitler, J. Maan, W. G. van der Wiel, G. Rijnders, D. H. Blank, and H. Hilgenkamp, Nat. Mater. **6**, 493 (2007).

[6] P. Zubko, S. Gariglio, M. Gabay, P. Ghosez, and J.-M. Triscone, Annu. Rev. Condens. Matter Phys. **2**, 141 (2011).

[7] H. Y. Hwang, Y. Iwasa, M. Kawasaki, B. Keimer, N. Nagaosa, and Y. Tokura, Nat. Mater. **11**, 103 (2012).

[8] S. Stemmer and S. James Allen, Annu. Rev. Mater. Res. **44**, 151 (2014).

[9] Y.-Y. Pai, A. Tylan-Tyler, P. Irvin, and J. Levy, Rep. Prog. Phys. **81**, 036503 (2018).

[10] J. Chakhalian, J. W. Freeland, A. J. Millis, C. Panagopoulos, and J. M. Rondinelli, Rev. Mod. Phys. **86**, 1189 (2014).

[11] F. Trier, D. V. Christensen, and N. Pryds, J. Phys. D: Appl. Phys. **51**, 293002 (2018).

[12] G. Samara and B. Morosin, Phys. Rev. B **8**, 1256 (1973).

[13] S. Harashima, C. Bell, M. Kim, T. Yajima, Y. Hikita, and H. Y. Hwang, Phys. Rev. B **88**, 085102 (2013).

[14] K. Ueno, S. Nakamura, H. Shimotani, H. Yuan, N. Kimura, T. Nojima, H. Aoki, Y. Iwasa, and M. Kawasaki, Nat. Nanotechnol. **6**, 408 (2011).

[15] C. Liu, X. Yan, D. Jin, Y. Ma, H.-W. Hsiao, Y. Lin, T. M. Bretz-Sullivan, X. Zhou, J. Pearson, B. Fisher, J. S. Jiang, W. Han, J.-M. Zuo, J. Wen, D. D. Fong, J. Sun, H. Zhou, and A. Bhattacharya, Science **371**, 716 (2021).

[16] H. Nakamura and T. Kimura, Phys. Rev. B **80**, 121308(R) (2009).

[17] P. D. C. King, R. H. He, T. Eknapakul, P. Buaphet, S.-K. Mo, Y. Kaneko, S. Harashima, Y. Hikita, M. S. Bahramy, C. Bell, Z. Hussain, Y. Tokura, Z. X. Shen, H. Y. Hwang, F. Baumberger, and W. Meevasana, Phys. Rev. Lett. **108**, 117602 (2012).

[18] K. V. Shanavas and S. Satpathy, Phys. Rev. Lett. **112**, 086802 (2014).

[19] K. Zou, S. Ismail-Beigi, K. Kisslinger, X. Shen, D. Su, F. Walker, and C. Ahn, APL Mater. **3**, 036104 (2015).

[20] J. Thompson, J. Hwang, J. Nichols, J. G. Connell, S. Stemmer, and S. S. A. Seo, Appl. Phys. Lett. **105**, 102901 (2014).

[21] H. Zhang, Y. Yun, X. Zhang, H. Zhang, Y. Ma, X. Yan, F. Wang, G. Li, R. Li, T. Khan *et al.*, Phys. Rev. Lett. **121**, 116803 (2018).

[22] H. Zhang, X. Yan, X. Zhang, S. Wang, C. Xiong, H. Zhang, S. Qi, J. Zhang, F. Han, N. Wu *et al.*, ACS Nano **13**, 609 (2019).

[23] H. Zhang, Y. Ma, H. Zhang, X. Chen, S. Wang, G. Li, Y. Yun, X. Yan, Y. Chen, F. Hu *et al.*, Nano Lett. **19**, 1605 (2019).

[24] N. Wadehra, R. Tomar, R. Gopal, Y. Singh, S. Dattagupta, and S. Chakraverty, Nat. Commun. **11**, 874 (2020).

[25] N. Kumar, N. Wadehra, R. Tomar, S. Dattagupta, S. Kumar, and S. Chakraverty, Adv. Quantum Technol. **4**, 2000081 (2020).

[26] A. F. Santander-Syro, C. Bareille, F. Fortuna, O. Copie, M. Gabay, F. Bertran, A. Taleb-Ibrahimi, P. Le Fèvre, G. Herranz, N. Reyren, M. Bibes, A. Barthelemy, P. Lecoeur, J. Guevara, and M. J. Rozenberg, Phys. Rev. B **86**, 121107(R) (2012).

[27] F. Y. Bruno, S. McKeown Walker, S. Riccò, A. De La Torre, Z. Wang, A. Tamai, T. K. Kim, M. Hoesch, M. S. Bahramy, and F. Baumberger, Adv. Electron. Mater. **5**, 1800860 (2019).

[28] S. K. Ojha, S. K. Gogoi, M. M. Patidar, R. K. Patel, P. Mandal, S. Kumar, R. Venkatesh, V. Ganesan, M. Jain, and S. Middey, Adv. Quantum Technol. **3**, 2000021 (2020).

[29] A. Fert, N. Reyren, and V. Cros, Nat. Rev. Mater. **2**, 17031 (2017).

[30] N. Nakagawa, H. Y. Hwang, and D. A. Muller, Nat. Mater. **5**, 204 (2006).

[31] M. Sing, G. Berner, K. Goß, A. Müller, A. Ruff, A. Wetscherek, S. Thiel, J. Mannhart, S. A. Pauli, C. W. Schneider, P. R. Willmott, M. Gorgoi, F. Schafers, and R. Claessen, Phys. Rev. Lett. **102**, 176805 (2009).

[32] G. Herranz, M. Basletić, M. Bibes, C. Carrétéro, E. Tafra, E. Jacquet, K. Bouzehouane, C. Deranlot, A. Hamzić, J.-M. Broto *et al.*, Phys. Rev. Lett. **98**, 216803 (2007).

[33] A. Kalabukhov, R. Gunnarsson, J. Börjesson, E. Olsson, T. Claeson, and D. Winkler, Phys. Rev. B **75**, 121404(R) (2007).

[34] J. Park, B.-G. Cho, K. D. Kim, J. Koo, H. Jang, K.-T. Ko, J.-H. Park, K.-B. Lee, J.-Y. Kim, D. R. Lee, C. A. Burns, S. S. A. Seo, and H. N. Lee, Phys. Rev. Lett. **110**, 017401 (2013).

[35] M. von Soosten, D. V. Christensen, C.-B. Eom, T. S. Jespersen, Y. Chen, and N. Pryds, Sci. Rep. **9**, 18005 (2019).

[36] M. Salluzzo, S. Gariglio, X. Torrelles, Z. Ristic, R. Di Capua, J. Drnec, M. M. Sala, G. Ghiringhelli, R. Felici, and N. Brookes, Adv. Mater. **25**, 2333 (2013).

[37] E. Breckenfeld, N. Bronn, J. Karthik, A. R. Damodaran, S. Lee, N. Mason, and L. W. Martin, Phys. Rev. Lett. **110**, 196804 (2013).

[38] S. Middey, C. Meneghini, and S. Ray, Appl. Phys. Lett. **101**, 042406 (2012).

[39] P. Giannozzi, O. Andreussi, T. Brumme, O. Bunau, M. B. Nardelli, M. Calandra, R. Car, C. Cavazzoni, D. Ceresoli, M. Cococcioni *et al.*, J. Phys.: Condens. Matter **29**, 465901 (2017).

[40] J. P. Perdew, K. Burke, and M. Ernzerhof, Phys. Rev. Lett. **77**, 3865 (1996).

[41] J. Heyd, G. E. Scuseria, and M. Ernzerhof, J. Chem. Phys. **124**, 219906 (2006).

[42] D. R. Hamann, Phys. Rev. B **88**, 085117 (2013).

[43] M. Schlipf and F. Gygi, Comput. Phys. Commun. **196**, 36 (2015).

[44] P. Scherpelz, M. Govoni, I. Hamada, and G. Galli, J. Chem. Theory Comput. **12**, 3523 (2016).

[45] M. V. Ivanov, T. V. Perevalov, V. S. Aliev, V. A. Gritsenko, and V. V. Kaichev, J. Appl. Phys. **110**, 024115 (2011).

[46] C. Ang, A. S. Bhalla, and L. E. Cross, Phys. Rev. B **64**, 184104 (2001).

[47] O. Aktas, S. Crossley, M. A. Carpenter, and E. K. H. Salje, Phys. Rev. B **90**, 165309 (2014).

[48] A. Verma, A. P. Kajdos, T. A. Cain, S. Stemmer, and D. Jena, Phys. Rev. Lett. **112**, 216601 (2014).

[49] J. Suntivich, W. T. Hong, Y.-L. Lee, J. M. Rondinelli, W. Yang, J. B. Goodenough, B. Dabrowski, J. W. Freeland, and Y. Shao-Horn, J. Phys. Chem. C **118**, 1856 (2014).

[50] D. D. Sarma, N. Shanthi, and P. Mahadevan, Phys. Rev. B **54**, 1622 (1996).

[51] See Supplemental Material at http://link.aps.org/supplemental/10.1103/PhysRevB.103.085120 for results of DFT+U calculations, results of larger supercell calculations, details of HSE calculations, comparison of defect formation energies, band structure of divacancy configuration A and C, band structure for charged defect state +1 and +2.

[52] K. Kuepper, A. V. Postnikov, A. Moewes, B. Schneider, M. Matteucci, H. Hesse, and M. Neumann, J. Phys.: Condens. Matter **16**, 8213 (2004).

[53] D. Kan, T. Terashima, R. Kanda, A. Masuno, K. Tanaka, S. Chu, H. Kan, A. Ishizumi, Y. Kanemitsu, Y. Shimakawa *et al.*, Nat. Mater. **4**, 816 (2005).

[54] M. L. Crespillo, J. T. Graham, F. Agulló-López, Y. Zhang, and W. J. Weber, J. Phys. D **50**, 155303 (2017).

[55] W. Xu, J. Yang, W. Bai, K. Tang, Y. Zhang, and X. Tang, J. Appl. Phys. **114**, 154106 (2013).

[56] J. Ravichandran, W. Siemons, M. L. Scullin, S. Mukerjee, M. Huijben, J. E. Moore, A. Majumdar, and R. Ramesh, Phys. Rev. B **83**, 035101 (2011).

[57] J. Ravichandran, W. Siemons, H. Heijmerikx, M. Huijben, A. Majumdar, and R. Ramesh, Chem. Mater. **22**, 3983 (2010).

[58] S. Wemple, Phys. Rev. **137**, A1575 (1965).

[59] I. Katayama and K. Tanaka, J. Phys. Soc. Jpn. **75**, 064713 (2006).

[60] S. Li, J. Luo, J. Liu, and J. Tang, J. Phys. Chem. Lett. **10**, 1999 (2019).

[61] D. Menzel, Appl. Phys. A **51**, 163 (1990).

[62] R. Scholz, A. Y. Kobitski, D. R. T. Zahn, and M. Schreiber, Phys. Rev. B **72**, 245208 (2005).

[63] R. Eglitis, E. Kotomin, G. Borstel, S. Kapphan, and V. Vikhnin, Comput. Mater. Sci. **27**, 81 (2003).

[64] S. Mochizuki, F. Fujishiro, and S. Minami, J. Phys.: Condens. Matter **17**, 923 (2005).

[65] J. Xi, H. Xu, Y. Zhang, and W. J. Weber, Phys. Chem. Chem. Phys. **19**, 6264 (2017).

[66] I. I. Tupitsyn, A. Deineka, V. A. Trepakov, L. Jastrabik, and S. E. Kapphan, Phys. Rev. B **64**, 195111 (2001).

[67] D. J. Singh, Phys. Rev. B **53**, 176 (1996).

[68] F. X. Zhang, J. Xi, Y. Zhang, Y. Tong, H. Xue, R. Huang, C. Trautmann, and W. J. Weber, J. Phys.: Condens. Matter **30**, 145401 (2018).

[69] M. Setvin, M. Reticcioli, F. Poelzleitner, J. Hulva, M. Schmid, L. A. Boatner, C. Franchini, and U. Diebold, Science **359**, 572 (2018).

[70] D. A. Muller, N. Nakagawa, A. Ohtomo, J. L. Grazul, and H. Y. Hwang, Nature (London) **430**, 657 (2004).

[71] D. D. Cuong, B. Lee, K. M. Choi, H.-S. Ahn, S. Han, and J. Lee, Phys. Rev. Lett. **98**, 115503 (2007).

[72] N. Shanthi and D. D. Sarma, Phys. Rev. B **57**, 2153 (1998).

[73] K. Eom, E. Choi, M. Choi, S. Han, H. Zhou, and J. Lee, J. Phys. Chem. Lett. **8**, 3500 (2017).

[74] C. Freysoldt, B. Grabowski, T. Hickel, J. Neugebauer, G. Kresse, A. Janotti, and C. G. Van de Walle, Rev. Mod. Phys. **86**, 253 (2014).

[75] R. Astala and P. D. Bristowe, Modell. Simul. Mater. Sci. Eng. **9**, 415 (2001).

[76] R. Eglitis and S. Piskunov, Comput. Condens. Matter **7**, 1 (2016).

[77] M. Moretti Sala, V. Bisogni, C. Aruta, G. Balestrino, H. Berger, N. B. Brookes, G. M. d. Luca, D. Di Castro, M. Grioni, M. Guarise *et al.*, New J. Phys. **13**, 043026 (2011).

[78] G. Makov and M. C. Payne, Phys. Rev. B **51**, 4014 (1995).

[79] C. Freysoldt, J. Neugebauer, and C. G. Van de Walle, Phys. Rev. Lett. **102**, 016402 (2009).

[80] H.-P. Komsa, T. T. Rantala, and A. Pasquarello, Phys. Rev. B **86**, 045112 (2012).

[81] M. Jain, J. R. Chelikowsky, and S. G. Louie, Phys. Rev. Lett. **107**, 216803 (2011).

[82] A. Malashevich, M. Jain, and S. G. Louie, Phys. Rev. B **89**, 075205 (2014).

[83] T. Biswas and M. Jain, Phys. Rev. B **99**, 144102 (2019).

[84] S. Kundu, M. H. Naik, and M. Jain, Phys. Rev. Mater. **4**, 054004 (2020).

[85] M. Choi, F. Oba, and I. Tanaka, Phys. Rev. B **83**, 214107 (2011).

[86] A. Lopez-Bezanilla, P. Ganesh, and P. B. Littlewood, Phys. Rev. B **92**, 115112 (2015).